Lithium whisker growth and stress generation in an in situ atomic force microscope–environmental transmission electron microscope set-up

Liqiang Zhang[1,2,6], Tingting Yang[1,6], Congcong Du[1], Qiunan Liu[1], Yushu Tang[2], Jun Zhao[1], Baolin Wang[3], Tianwu Chen[4], Yong Sun[1], Peng Jia[1], Hui Li[1], Lin Geng[1], Jingzhao Chen[1], Hongjun Ye[1], Zaifa Wang[1], Yanshuai Li[1], Haiming Sun[1], Xiaomei Li[1], Qiushi Dai[1], Yongfu Tang[1]*, Qiuming Peng[1], Tongde Shen[1], Sulin Zhang[4]*, Ting Zhu[3]* and Jianyu Huang[1,5]*

Lithium metal is considered the ultimate anode material for future rechargeable batteries[1,2], but the development of Li metal-based rechargeable batteries has achieved only limited success due to uncontrollable Li dendrite growth[3–7]. In a broad class of all-solid-state Li batteries, one approach to suppress Li dendrite growth has been the use of mechanically stiff solid electrolytes[8,9]. However, Li dendrites still grow through them[10,11]. Resolving this issue requires a fundamental understanding of the growth and associated electro-chemo-mechanical behaviour of Li dendrites. Here, we report in situ growth observation and stress measurement of individual Li whiskers, the primary Li dendrite morphologies[12]. We combine an atomic force microscope with an environmental transmission electron microscope in a novel experimental set-up. At room temperature, a submicrometre whisker grows under an applied voltage (overpotential) against the atomic force microscope tip, generating a growth stress up to 130 MPa; this value is substantially higher than the stresses previously reported for bulk[13] and micrometre-sized Li[14]. The measured yield strength of Li whiskers under pure mechanical loading reaches as high as 244 MPa. Our results provide quantitative benchmarks for the design of Li dendrite growth suppression strategies in all-solid-state batteries.

Figure 1a–c shows the in situ electro-chemo-mechanical experiment for observing and measuring individual Li whiskers through an atomic force microscope with an environmental transmission electron microscope (AFM–ETEM) set-up, which consists of a Li metal electrode, a Li_2CO_3 solid electrolyte and a silicon AFM tip as a counter electrode. The Li_2CO_3 electrolyte was formed as a thin layer covering the Li metal surface due to reaction between Li and CO_2 gas in the ETEM chamber[15] (Supplementary Fig. 1). As soon as the AFM tip was brought into contact with the Li_2CO_3 surface and a negative potential was applied between the AFM tip and Li electrode, individual straight Li whiskers sprouted out between the AFM tip and the Li_2CO_3/Li substrate (Fig. 1d, Supplementary Figs. 2 and 3 and Supplementary Videos 1 and 2). The relatively slow lithiation of the Si AFM tip facilitated plating of Li in the form of Li whiskers.

During this process, the Li metal substrate and the Li whisker effectively acted as two opposite electrodes of a symmetric Li cell, with the Li_2CO_3 surface layer as a solid electrolyte between the two Li electrodes. The growing Li whisker pushed the AFM tip upwards, thus permitting real-time measurement of the stress generated in the Li whisker (Methods).

To facilitate the whisker nucleation, an arc-discharged multiwall carbon nanotube (CNT) was attached to the AFM tip in the ETEM. Before the growth of a straight Li whisker, a single Li spheroid first nucleated at the contact point between the CNT and the Li_2CO_3/Li substrate, and then grew along the CNT (Fig. 1d, 1,863 s, Supplementary Figs. 2 and 3 and Supplementary Videos 1 and 2). Under a constant bias voltage, the spheroid grew to about 1.26 μm in diameter and subsequently necked downwards to form a straight rod-like whisker (Fig. 1d, 2,028 s). The upper end of the Li whisker, which was in contact with the AFM tip, remained geometrically unchanged during the whisker growth process (Fig. 1d, 2,028 s and 2,119 s). This indicates a root-growth mode[3,16] through Li deposition at the contact interface between the lower end of the Li whisker and the Li_2CO_3/Li substrate. After 2,119 s, the length of the overall straight Li whisker reached 4.08 μm (Fig. 1d). Attachment of a CNT to the AFM tip facilitates the whisker nucleation but is not a prerequisite, since whiskers can also nucleate without the aid of a CNT (Supplementary Figs. 4–8 and Supplementary Videos 3–7). The morphology of the whisker resembles that of a mushroom (Supplementary Fig. 9). A similar morphology was also observed from Li whiskers grown in liquid electrolytes[3,17], where a whisker nucleated from a spherical bud and then grew in length.

Importantly, we found that during the Li growth process, a layer of Li_2CO_3 (~5–20 nm thick) quickly covered the surface of a growing whisker, owing to the presence of CO_2 gas inside the ETEM chamber (Supplementary Figs. 1 and 10). Such an ultrathin Li_2CO_3 layer plays a critical role in stabilizing the Li whisker and preventing its damage by the electron beam (Methods and Supplementary Fig. 11), thereby enabling in situ imaging and stress measurement inside the ETEM.

[1]Clean Nano Energy Center, State Key Laboratory of Metastable Materials Science and Technology, Yanshan University, Qinhuangdao, China. [2]State Key Laboratory of Heavy Oil Processing, China University of Petroleum Beijing, Beijing, China. [3]Woodruff School of Mechanical Engineering, Georgia Institute of Technology, Atlanta, GA, USA. [4]Department of Engineering Science and Mechanics, Pennsylvania State University, University Park, PA, USA. [5]Key Laboratory of Low Dimensional Materials and Application Technology of Ministry of Education, School of Materials Science and Engineering, Xiangtan University, Xiangtan, China. [6]These authors contributed equally: Liqiang Zhang, Tingting Yang. *e-mail: tangyongfu@ysu.edu.cn; suz10@engr.psu.edu; ting.zhu@me.gatech.edu; jyhuang8@hotmail.com
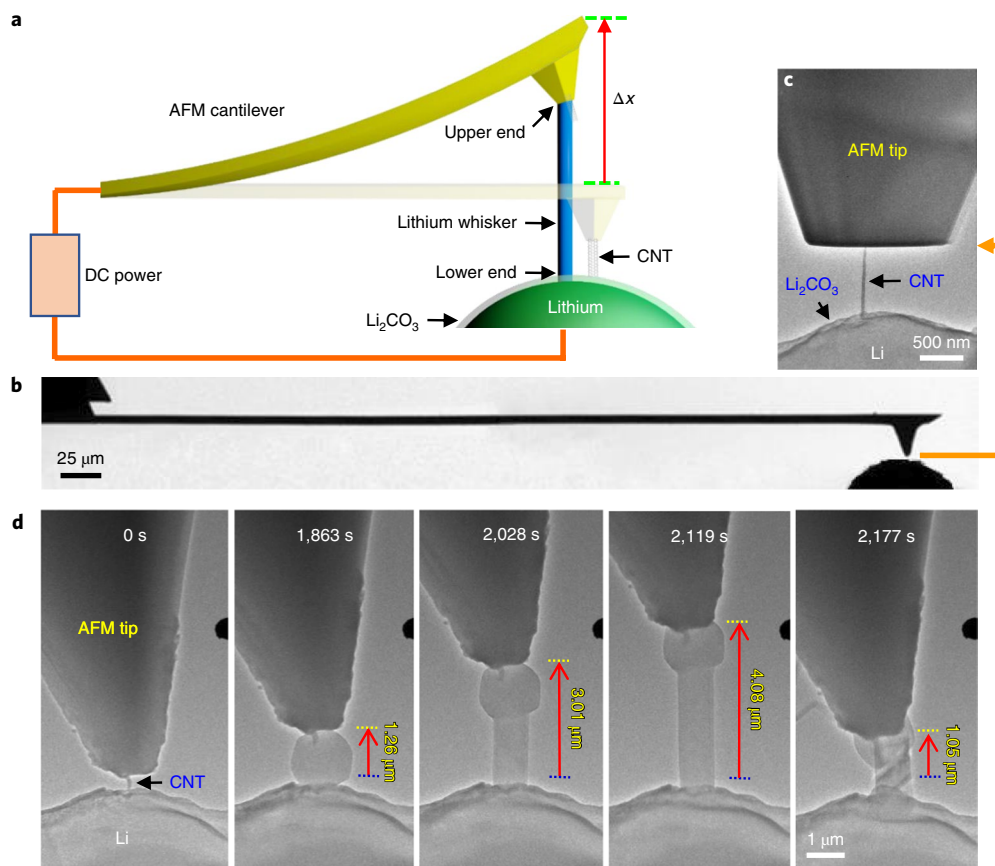
Fig. 1 | In situ AFM–ETEM characterization of stress generation during Li whisker growth. a, Schematic of the AFM–ETEM set-up used for observation and measurement of Li whisker growth. An arc-discharged CNT was attached to a conducting AFM tip by electron beam deposition of carbonaceous materials, and this assembly was used as a cathode; the scratched Li metal on the top of a sharp tungsten needle was used as an anode; and the naturally formed Li_2CO_3 on the Li surface was used as a solid electrolyte. The measured displacement of the cantilever tip is denoted as Δx. **b**, TEM image showing an AFM cantilever approaching the counter electrode of Li metal. **c**, TEM image showing a CNT attached to a flattened AFM tip. **d**, Time-lapse TEM images of Li whisker growth. A nano-sized Li ball nucleated from the CNT, Li_2CO_3 and gas triple point (at 1,863 s), and it grew with an increase of applied potential. As the Li ball grew to about 1.26 μm in size, a whisker emerged underneath the ball (at 2,028 s), which pushed the AFM cantilever up, thus generating the axially compressive stress in the whisker. The spring constant of the Si AFM cantilever beam is $k = 3\,\text{N}\,\text{m}^{-1}$ in this case. When the whisker reached 4.08 μm in length, it collapsed (at 2,177 s) due to axial compression by the AFM tip. The blue dotted line indicates a fixed reference position, and the red arrow indicates the upward displacement of the AFM tip.

The Li whiskers had a body-centred cubic lattice structure and grew preferably along certain crystallographic directions. The growth directions of <001> (Supplementary Fig. 12 and Supplementary Video 8), <112> (Supplementary Fig. 13 and Supplementary Video 9), <110> (Supplementary Fig. 14 and Supplementary Video 10) and <111> (Supplementary Fig. 15 and Supplementary Video 11) were observed, but the <111> and <112> directions occurred predominantly.

The whisker growth process can be typically separated into three stages. In stage I, a Li spheroid nucleated at the interface between the AFM tip and Li_2CO_3/Li substrate (for example, Fig. 2a, 261 s, Supplementary Fig. 16 and Supplementary Videos 12 and 13), as described earlier. The diameter of the Li spheroids, such as those shown in Supplementary Fig. 16, follows a square-root relationship with growth time (Supplementary Fig. 17), indicating a diffusion-controlled growth process.

In stage II, the Li whisker started to grow in length without an appreciable change in diameter (Fig. 2a, 282 s, and Supplementary Video 13). As the AFM tip was pushed up continuously, the axial compressive stress increased gradually in the Li whisker. Under a given applied voltage, ϕ_a, the whisker ceased to grow as it reached a certain length (Fig. 2c, from 445 s to 482 s, Supplementary Figs. 18

and 19 and Supplementary Videos 14–16). The corresponding critical stress is denoted by $\tilde{\sigma}$ (being positive for compression). An increase of applied voltage, ϕ_a, led to further growth of the whisker, resulting in an increase in the critical stress, $\tilde{\sigma}$, as the whisker growth stopped again (Fig. 2c, from 482 s to 595 s, Supplementary Figs. 18 and 19 and Supplementary Videos 14–16). Figure 2d shows the stress, $\tilde{\sigma}$, versus applied voltage, ϕ_a, in stage II for several whiskers. As shown in the Supplementary Discussion, the applied voltage, ϕ_a, raises the overpotential that drives the Li whisker growth, and the stress, $\tilde{\sigma}$, in the Li whisker scales linearly with the overpotential[18] by

$$\tilde{\sigma} V_m = F\Delta\phi \tag{1}$$

where $\Delta\phi$ is the overpotential across the contact interface between the Li whisker and Li_2CO_3/Li substrate, F is Faraday's constant ($F = 9.65 \times 10^4\,\text{C}\,\text{mol}^{-1}$) and V_m is the molar volume of Li metal ($V_m = 13\,\text{cm}^3\,\text{mol}^{-1}$). Equation (1) represents an energy balance on Li insertion at the contact interface and thus on the growth of the Li whisker. Namely, Li insertion is driven by the overpotential, but is resisted by the mechanical stress. Under a given $\Delta\phi$, the growth rate of a Li whisker vanishes when the electrical work, $F\Delta\phi$, is counter
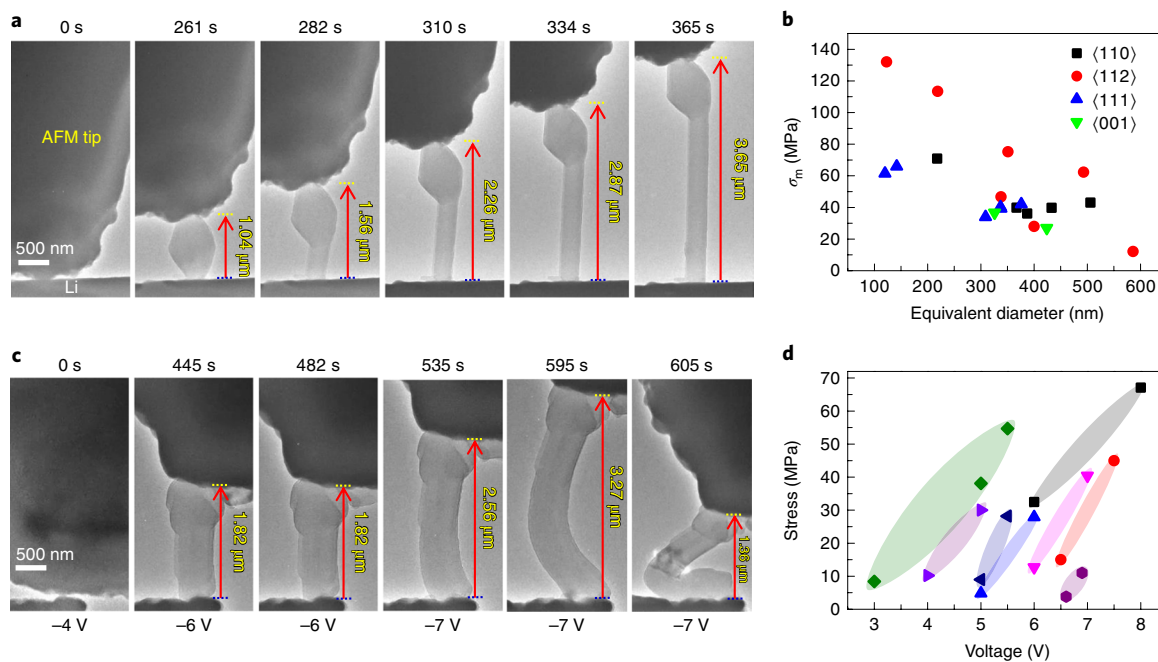
Fig. 2 | In situ AFM–ETEM imaging of Li whisker growth and concurrent measurement of the maximum stress in Li whiskers under applied voltages.
a, A Li ball with size of 568 nm nucleated underneath the AFM tip without CNT (261 s) and then necked down to form a whisker (282 s, 310 s, 365 s) ($k = 0.2$ N m^{-1}). The whisker growth ceased due to compression imposed by the AFM cantilever tip under an applied potential. **b**, Plot of the maximum stress σ_m versus equivalent diameter for Li whiskers with different growth directions. The equivalent diameter refers to the diameter of a circle whose area is equivalent to the cross-sectional area of a Li whisker. **c**, A whisker grew at an applied potential of −6 V (445 s), and its growth ceased at a prolonged time (482 s) ($k = 3$ N m^{-1}). The whisker resumed its growth as the applied potential increased to −7 V (535 s, 595 s), causing the bending instability (595 s) and eventual collapse of the whisker (605 s). **d**, Critical compressive stress (when the growth of a Li whisker stops) versus applied voltage for eight Li whiskers tested. Each elongated oval encloses the data points measured for a whisker, and thus serves as a guide to the eye to distinguish different sets of data for different whiskers.

balanced by the mechanical work, $\widetilde{\sigma}V_m$. According to equation (1), an overpotential, $\Delta\phi$, of 10 mV gives rise to a growth stress of about 75 MPa. However, in our experiment such a level of stress was generated by the applied voltage of the order of a few volts. These results indicate that the overpotential responsible for whisker growth can only be a small fraction of the applied voltage, and major potential drops should have occurred at regions other than the contact interface between the Li whisker and Li$_2$CO$_3$/Li substrate. Indeed, our measurements show electrical resistances at the giga-ohm level from the AFM tip region as well as from the Li$_2$CO$_3$ layer on the Li metal, which are 10^9 times higher than the resistance of the Li whisker itself. Hence, these regions with high resistances are responsible for large potential drops (see a discussion of the relationship between stress and overpotential in the Supplementary Discussion, including Supplementary Figs. 20 and 21).

In stage III, the whisker no longer grew longitudinally as the applied voltage increased, but was often bent abruptly to collapse (Fig. 2c, from 595 s to 605 s, and Supplementary Video 16). This buckling instability was caused by a large axial compressive load on the slender whisker. The corresponding compressive stress at the instability point (for example, Fig. 2c, 595 s) is denoted as the maximum stress, σ_m, for stable growth of a Li whisker without lateral constraints. We measured σ_m for a number of Li whiskers with different diameters and crystallographic directions. The maximum stresses vary from tens of MPa to over 130 MPa and exhibit a clear size dependence (Fig. 2b), that is, the smaller the whisker diameter, the higher the maximum stress, σ_m. This trend can be understood by an elastic buckling analysis with consideration of the AFM cantilever stiffness k, which yields a scaling relation of $\sigma_m \approx E^{1/3}(k/d)^{2/3}$, where E and d denote the Young's modulus and diameter of the Li

whisker, respectively. In addition, we note that the maximum stress, σ_m, obtained during in situ Li whisker growth is much higher than that of Li spheres measured by nanoindentation[19], and is also higher than that of Li micropillars (~100 MPa)[14].

The above measurements indicate that high stresses up to 130 MPa can be built up in Li whiskers under an applied voltage and axial constraint. However, further increase of stress in a whisker towards its plastic yielding could not be directly achieved by increasing the applied voltage, as it would cause the buckling instability and even short circuiting. This issue arises due to the absence of lateral constraints to a growing whisker. Imposing lateral constraints is possible, but it would block electron beams and encumber TEM observations. In contrast, in all-solid-state Li batteries, a growing whisker within a solid electrolyte is generally subjected to three-dimensional constraints from the surrounding electrolyte and thus probably generates sufficiently high stresses to initiate plastic deformation. To study the elasto-plastic response of Li whiskers, we conducted in situ mechanical compression tests on as-grown Li whiskers without applied voltage. This enabled us to control the axial compressive load well and thus measure the yield strength, σ_Y, of Li whiskers.

Figure 3a–f presents a series of TEM images of in situ compression of a single Li whisker at room temperature with a strain rate of about 1×10^{-3} s^{-1}. During a typical in situ test, the compressed whisker was gradually pushed upwards against the AFM tip until plastic yielding occurred (Fig. 3b–e), as evidenced by the formation of an inclined shear band (Fig. 3e). Further compression eventually triggered the collapse of the Li whisker (Fig. 3f). Supplementary Figs. 22 and 23 (Supplementary Videos 17 and 18) show two additional compression experiments of as-grown Li whiskers. Figure 3g
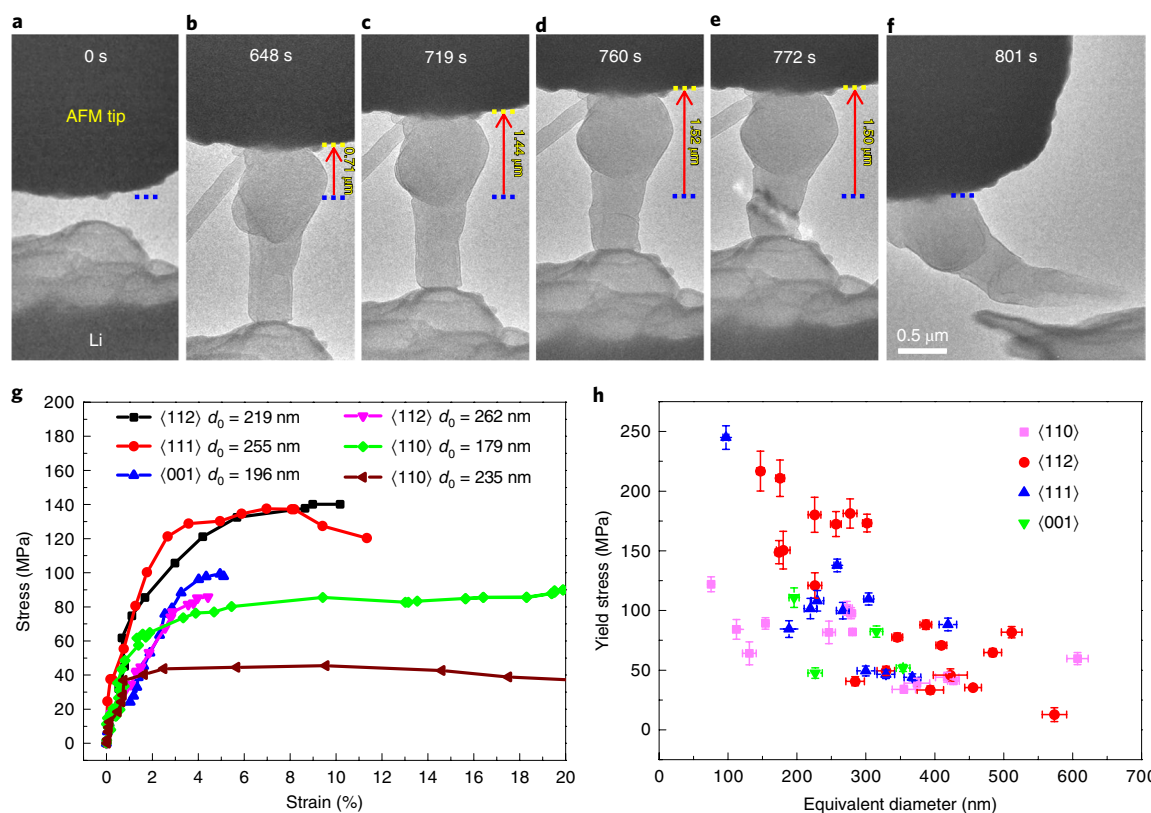
Fig. 3 | In situ compression testing of as-grown Li whiskers. Metal Li was manipulated to approach the AFM tip (**a**); a growing Li whisker pushed up against the AFM tip (**b–e**) ($k = 6\,\mathrm{N\,m^{-1}}$); and this whisker collapsed after extensive compression (**f**). The blue dotted line indicates a fixed reference position, and the red arrow indicates the upward displacement of the AFM tip. **g**, Compressive stress–strain curves of six whiskers with different growth directions and diameters d_0. **h**, Yield stress versus equivalent diameter measured for Li whiskers with different growth directions. The vertical and horizontal error bars show the standard deviations of yield stress and equivalent diameter, respectively. The yield stress is the critical stress at which the whisker can be continuously compressed but the applied force by the AFM tip is not increased. The equivalent diameter corresponds to the diameter of a circle whose area is equivalent to the cross-sectional area of the Li whisker.

shows several representative stress–strain curves, which exhibit an elastic regime with the elastic strain limit less than 4%, as well as an extensive plastic regime with slight strain hardening. The plastic strain can even reach over 20%. The Young's modulus, E, calculated from the slope of the stress–strain curve varies from 2.7 to 21 GPa. Such a large spread of measured E arises due to the difficulty in accurately measuring small elastic strains, which has been a challenge for nanomechanical testing in general[20]. The yield strength, σ_Y, obtained varies from 12.2 MPa to 244 MPa (Fig. 3h), exhibiting a sample size effect, that is, smaller being stronger. The maximum value of σ_Y is much higher than that of σ_m for Li whiskers. The spread of measured σ_Y can be attributed to the statistical nature of dislocation source strengths in small-volume metallic materials[20]. In the analysis of elasto-plastic phenomena, the yield strength, σ_Y, measured from uniaxial loading is commonly used to determine the attainment of plastic yielding under multiaxial stresses on the basis of the von Mises (J_2) plasticity theory[21]. In the same spirit, one can use the measured yield strength, σ_Y, to analyse plastic yielding for the Li whisker that grows inside a solid electrolyte and thus experiences multiaxial stresses.

It has been reported that the Young's modulus of bulk polycrystalline Li is about 4.3 to 8 GPa (refs. [13,22–24]), and its yield strength is between 0.4 and 0.9 MPa (refs. [13,25]). The yield strengths of Li whiskers measured here range from 12.2 to 244 MPa, which are two orders of magnitude higher than that of bulk polycrystalline Li. The Young's moduli of Li whiskers measured here are between 2.7 and 21 GPa, much lower than those of a solid electrolyte, such as $Li_7La_3Zr_2O_{12}$

($\sim$150 GPa)[26,27]. On the basis of the Monroe–Newman theory[9,28], the growth of Li whiskers may be suppressed by a stiff solid electrolyte due to inhibition of surface roughening of Li metal, as its Young's modulus is significantly lower than that of $Li_7La_3Zr_2O_{12}$. However, short circuiting was still observed in $Li_7La_3Zr_2O_{12}$-based all-solid-state batteries, which indicates that mechanisms other than surface roughening are operating. To resolve the above contradiction, Porz et al.[18] suggested an alternative mechanism of Li dendrite formation and growth through the solid electrolyte[10,29,30]. Specifically, small pores or cracks are generally present on the solid electrolyte surface, and these surface flaws will be filled by Li metal deposition under overpotentials. Mechanical stresses within both the deposited Li metal and surrounding solid electrolyte rise with continual Li plating. Such stress build-up may cause the growth of surface flaws and thus the formation of a main crack, leading to Li dendrite growth. The measured elasto-plastic behaviour of Li whiskers in this work indicates a limitation of the dendrite growth model of Porz et al.[18], which assumes a purely elastic response of the Li dendrite during its growth in the solid electrolyte. On the basis of the measured elasto-plastic responses of Li whiskers, we further developed a model showing how an elasto-plastic Li whisker might penetrate an elastically stiff solid electrolyte. The resulting whisker growth map (Supplementary Discussion and Supplementary Fig. 24) demonstrates a significant impact of the elasto-plasticity of the Li whisker on its growth behaviour. It also underscores the importance of the development of solid electrolytes with high fracture toughness and minimized surface flaw size to effectively suppress

Li dendrite growth in all-solid-state batteries. Finally, we note that the current mechanical testing was conducted under a fairly high strain rate ($\sim 10^{-3}\,\mathrm{s}^{-1}$) compared to the typical loading rate during battery operation. The time-dependent electro-chemo-mechanical response of Li whiskers may affect their diffusional creep and infiltration behaviours within solid electrolytes[18], which can be further studied with this AFM–ETEM set-up in the future.

Note added in proof: At peer review stage, we became aware of a related work[31] showing Li whisker formation and growth under stress by a similar AFM–ETEM set-up.

Online content

Any methods, additional references, Nature Research reporting summaries, source data, extended data, supplementary information, acknowledgements, peer review information; details of author contributions and competing interests; and statements of data and code availability are available at https://doi.org/10.1038/s41565-019-0604-x.

References

1. Tarascon, J. M. & Armand, M. Issues and challenges facing rechargeable lithium batteries. *Nature* **414**, 359–367 (2001).
2. Xu, W. et al. Lithium metal anodes for rechargeable batteries. *Energy Environ. Sci.* **7**, 513–537 (2014).
3. Kushima, A. et al. Liquid cell transmission electron microscopy observation of lithium metal growth and dissolution: root growth, dead lithium and lithium flotsams. *Nano Energy* **32**, 271–279 (2017).
4. Lin, D., Liu, Y. & Cui, Y. Reviving the lithium metal anode for high-energy batteries. *Nat. Nanotechnol.* **12**, 194 (2017).
5. Guo, Y., Li, H. & Zhai, T. Reviving lithium-metal anodes for next-generation high-energy batteries. *Adv. Mater.* **29**, 1700007 (2017).
6. Wang, X. et al. Stress-driven lithium dendrite growth mechanism and dendrite mitigation by electroplating on soft substrates. *Nat. Energy* **3**, 227–235 (2018).
7. Li, L. et al. Self-heating–induced healing of lithium dendrites. *Science* **359**, 1513–1516 (2018).
8. Liu, Y. et al. Making Li-metal electrodes rechargeable by controlling the dendrite growth direction. *Nat. Energy* **2**, 17083 (2017).
9. Monroe, C. & Newman, J. The impact of elastic deformation on deposition kinetics at lithium/polymer interfaces. *J. Electrochem. Soc.* **152**, A396–A404 (2005).
10. Ren, Y., Shen, Y., Lin, Y. & Nan, C. W. Direct observation of lithium dendrites inside garnet-type lithium-ion solid electrolyte. *Electrochem. Commun.* **57**, 27–30 (2015).
11. Suzuki, Y. et al. Transparent cubic garnet-type solid electrolyte of Al_2O_3-doped $Li_7La_3Zr_2O_{12}$. *Solid State Ion.* **278**, 172–176 (2015).
12. Brenner, S. S. Growth and properties of 'whiskers': further research is needed to show why crystal filaments are many times as strong as large crystals. *Science* **128**, 569–575 (1958).
13. Schultz, R. P. *Lithium: Measurement of Young's Modulus and Yield Strength* (Fermi National Accelerator Laboratory, 2002).
14. Xu, C., Ahmad, Z., Aryanfar, A., Viswanathan, V. & Greer, J. R. Enhanced strength and temperature dependence of mechanical properties of Li at small scales and its implications for Li metal anodes. *Proc. Natl Acad. Sci. USA* **114**, 57–61 (2017).
15. Yang, T. T. et al. Air-stable lithium spheres produced by electrochemical plating. *Angew. Chem. Int. Ed. Engl.* **57**, 12750–12753 (2018).
16. Li, L., Li, S. & Lu, Y. Suppression of dendritic lithium growth in lithium metal-based batteries. *Chem. Commun.* **54**, 6648–6661 (2018).
17. Qian, J. et al. Dendrite-free Li deposition using trace-amounts of water as an electrolyte additive. *Nano Energy* **15**, 135–144 (2015).
18. Porz, L. et al. Mechanism of lithium metal penetration through inorganic solid electrolytes. *Adv. Energy Mater.* **7**, 1701003 (2017).
19. Xiang, B., Wang, L., Liu, G. & Minor, A. M. Electromechanical probing of Li/Li_2CO_3 core/shell particles in a TEM. *J. Electrochem. Soc.* **160**, A415–A419 (2013).
20. Greer, J. R. & De Hosson, J. T. M. Plasticity in small-sized metallic systems: intrinsic versus extrinsic size effect. *Prog. Mater. Sci.* **56**, 654–724 (2011).
21. Khan, A. S. & Huang, S. *Continuum Theory of Plasticity* (John Wiley & Sons, 1995).
22. Masias, A., Felten, N., Garcia-Mendez, R., Wolfenstine, J. & Sakamoto, J. Elastic, plastic, and creep mechanical properties of lithium metal. *J. Mater. Sci.* **54**, 2585–2600 (2019).
23. Bridgman, P. W. The effect of tension on the electrical resistance of certain abnormal metals. *Proc. Natl Acad. Sci. USA* **57**, 41–66 (1922).
24. Robertson, W. M. & Montgomery, D. J. Elastic modulus of isotopically-concentrated lithium. *Phys. Rev.* **117**, 440–442 (1959).
25. Tariq, S. et al. Li material testing–Fermilab antiproton source lithium collection lens. In *Proc. 2003 Particle Accelerator Conference* (eds Chew, J. et al.) 1452–1454 (IEEE, 2003).
26. Ni, J. E., Case, E. D., Sakamoto, J. S., Rangasamy, E. & Wolfenstine, J. B. Room temperature elastic moduli and Vickers hardness of hot-pressed LLZO cubic garnet. *J. Mater. Sci.* **47**, 7978–7985 (2012).
27. Wolfenstine, J. et al. A preliminary investigation of fracture toughness of $Li_7La_3Zr_2O_{12}$ and its comparison to other solid Li-ion conductors. *Mater. Lett.* **96**, 117–120 (2013).
28. Ferrese, A. & Newman, J. Mechanical deformation of a lithium-metal anode due to a very stiff separator. *J. Electrochem. Soc.* **161**, A1350–A1359 (2014).
29. Nagao, M. et al. In situ SEM study of a lithium deposition and dissolution mechanism in a bulk-type solid-state cell with a $Li_2S-P_2S_5$ solid electrolyte. *Phys. Chem. Chem. Phys.* **15**, 18600–18606 (2013).
30. Ansell, R. The chemical and electrochemical stability of beta-alumina. *J. Mater. Sci.* **21**, 365–379 (1986).
31. He, Y. et al. Origin of lithium whisker formation and growth under stress. *Nat. Nanotechnol.* **14**, 1042–1047 (2019).

Methods

AFM–ETEM set-up. To construct the AFM–ETEM testing device, we inserted a Si AFM cantilever beam (with the effective spring stiffness k in the range of 0.1–40 N m^{-1}) into one end of the AFM–ETEM holder (Fig. 1a–c). We welded a short CNT onto the AFM tip by e-beam-induced carbon deposition. After that, a piece of Li metal was mounted onto the other end of the TEM holder (Pico Femto FE-F20) inside a glovebox. Then, the holder was sealed in an airtight bag filled with dry argon and transferred into the ETEM. The total time of air exposure was less than 2 s, which limited the oxidation of metal Li. The movement of the sample was manipulated by the piezoelectric tube of the holder. When the CNT and Li metal were connected, an external bias (−2 to −8 V) was supplied for growing Li whiskers. A growing Li whisker pushed the AFM tip upwards, thus permitting real-time measurements of the stress generated in the Li whisker. Specifically, given the effective spring constant, k, of the AFM cantilever, the force, P, generated by Li whisker growth was calculated from the measured displacement, Δx, of the cantilever tip by $P = k\Delta x$. Note that because the deflection of the cantilever (<5 μm) was much smaller than its beam length (520 μm), a linear relationship between Δx and P can be reasonably assumed. As the diameter and, accordingly, the cross-sectional area A of the whisker were measured through in situ TEM imaging, the axial compressive stress, σ, generated in the whisker was determined by $\sigma = P/A$. To accurately measure the cross-sectional area A, we rotated the Li whisker in the ETEM to determine its cross-sectional geometry (Supplementary Fig. 25). Sometimes, a Li whisker was reoriented with its cross-section facing the electron beam (Supplementary Fig. 26 and Supplementary Video 19), which permitted direct measurement of its cross-sectional area. During the experiment, a beam stopper was inserted into the field of view as the reference for displacement measurements of the Li whisker. We conducted additional benchmark experiments to determine the accuracy of our measurement system. That is, we first measured the mechanical strength of individual single-crystal Ag pillars with our AFM–ETEM system, and then tested similar Ag pillars with a commercial mechanical testing TEM sample holder (Hysitron PI 95). The results are shown in Supplementary Fig. 27. The measured yield strength, σ_y, was 366.0 MPa from the AFM–ETEM platform, while the measured σ_y was 349.2 MPa from the Hysitron PI 95 holder. The difference is about 4.6%, which provides a quantitative measure of the accuracy of our AFM–ETEM testing system. During whisker growth, the current in the whisker was recorded by an ampere meter, which read about 1.2×10^{-10} A (Supplementary Fig. 28). As the whisker has a diameter of about 700 nm, the current density is approximately 31 mA cm^{-2}, which is comparable to that in conventional Li-ion batteries[32].

Effect of CO$_2$ environment. The CO$_2$ gas environment in the ETEM plays a critical role in the formation of the passivation layer of Li whiskers, similar to the effect of an oxygen gas environment on the formation of the oxide passivation layer of Li whiskers[33]. We normally did not observe whisker growth without a CO$_2$ gas environment. Instead, only Li plates were formed (Supplementary Fig. 29). We found that Li whiskers formed only at CO$_2$ partial pressures between ~10^{-4} and 3 mbar (Supplementary Fig. 30). The typical thickness of Li$_2$CO$_3$ is less than 20 nm (Supplementary Fig. 31). For micrometre-diameter Li whiskers, such a thin Li$_2$CO$_3$ nanolayer should have a weak effect on their mechanical properties. For small samples with diameters of a few hundred nanometres, the yield strength of a composite Li/Li$_2$CO$_3$ whisker could be increased by up to about 20% compared to a pure Li whisker (Supplementary Fig. 32). Future study is needed to better quantify the effects of the surface Li$_2$CO$_3$ nanolayer.

Size effect of Li whiskers. Two sources can contribute to the measured sample size effect on the yield strength of Li whiskers: the intrinsic size effect (as discussed earlier) and the Li$_2$CO$_3$ nanolayer effect. For the latter effect, it is noted that the yield strength of the Li$_2$CO$_3$ nanolayer is generally higher than that of the pure Li whisker. For smaller Li whiskers, the cross-sectional areal fraction of the Li$_2$CO$_3$ nanolayer is higher, giving rise to a higher yield strength. The size effect due to the Li$_2$CO$_3$ nanolayer becomes negligibly small as the diameter of the Li whisker increases to a few hundred nanometres. While the mechanical properties of submicrometre Li whiskers are the focus of this work, the mechanical properties of Li from micrometre scale to bulk are also compared in the Supplementary Materials (Supplementary Figs. 33 and 34), which confirms the intrinsic size effect for Li whiskers from the nanometre to millimetre scale, namely, smaller being stronger.

References

32. Bai, P. et al. Interactions between lithium growths and nanoporous ceramic separators. *Joule* **2**, 2434–2449 (2018).
33. Yulaev, A. et al. From microparticles to nanowires and back: radical transformations in plated Li metal morphology revealed via in situ scanning electron microscopy. *Nano Lett.* **18**, 1644–1650 (2018).

Author contributions

L.Z., T.Y. and C.D. conceived the experiment. Q.L., Yushu Tang and J.Z. performed ETEM measurements. Y.S., P.J. and H.L. fabricated the AFM device. L.G., J.C. and H.Y. fabricated the carbon nanotube. Z.W., Y.L., H.S., X.L. and Q.D. conducted mechanical measurements. B.W. and T.C. performed computational modelling. Q.P., T.S., Yo Tang, S.Z., T.Z. and J.H. supervised the project. L.Z., T.Z. and J.H. wrote the paper. All authors discussed the results and commented on the manuscript.

Competing interests

The authors declare no competing interests.

Additional information

Supplementary information is available for this paper at https://doi.org/10.1038/s41565-019-0604-x.

Correspondence and requests for materials should be addressed to Y.T., S.Z., T.Z. or J.H.

Reprints and permissions information is available at www.nature.com/reprints.